Ultraviolet laser-induced fragmentation of hydrocarbon fuel droplets

RESEARCH ARTICLE | SEPTEMBER 16 2024

Ultraviolet laser-induced fragmentation of hydrocarbon fuel droplets

Vishal S. Jagadale ; Devashish Chorey ; Mats Andersson ; Devendra Deshmukh ; Dag Hanstorp ; Yogeshwar Nath Mishra

Physics of Fluids 36, 097127 (2024)
https://doi.org/10.1063/5.0223143

Physics of Fluids ARTICLE pubs.aip.org/aip/pof

Ultraviolet laser-induced fragmentation of hydrocarbon fuel droplets

Cite as: Phys. Fluids **36**, 097127 (2024); doi: 10.1063/5.0223143
Submitted: 12 June 2024 · Accepted: 26 August 2024 ·
Published Online: 16 September 2024

Vishal S. Jagadale,[1] Devashish Chorey,[1] Mats Andersson,[2] Devendra Deshmukh,[1,a)] Dag Hanstorp,[3,a)] and Yogeshwar Nath Mishra[3,4,b)]

AFFILIATIONS

[1]Spray and Combustion Laboratory, Department of Mechanical Engineering, Indian Institute of Technology Indore, Simrol, Madhya Pradesh 453552, India
[2]Department of Mechanics and Maritime Sciences, Chalmers University of Technology, Gothenburg, Sweden
[3]Department of Physics, University of Gothenburg, Gothenburg SE-41296, Sweden
[4]NASA-Jet Propulsion Laboratory, California Institute of Technology, Pasadena, California 91109, USA

[a)]**Authors to whom correspondence should be addressed:** dldeshmukh@iiti.ac.in and dag.hanstorp@physics.gu.se
[b)]**Present address:** Visual Computing Center, KAUST, Thuwal, Saudi Arabia.

ABSTRACT

The present study aims to understand droplet fragmentation due to instabilities from the radiative heating process. We focus on the plasma-induced breakup mechanism of iso-octane and n-hexane droplets from the nucleation of holes through sheets and instabilities. The plasma generation inside the droplets leads to an intense explosion followed by fragmentation of the droplets. A droplet is suspended in the air using an acoustic levitator and exposed to ultraviolet nanosecond laser pulses. The droplet sizes used are in the range of 0.5–2 mm in diameter, and laser energies are 10–20 mJ per pulse. Initially, plasma formation followed by shock wave emission is observed during the impact of the laser pulse. Afterward, the droplet opens at one side and is stretched vertically to form a liquid sheet. The hole formation and its rapid growth result in the breaking of the thin liquid sheet. Small droplets and ligaments emerge from the circular edge of the sheet, which follows the well-known ligament distribution. This study reveals the detailed analysis of expansion dynamics, evolution of single and multiple holes, and instabilities associated with the liquid sheet. The results observed are categorized into four different mechanisms: (1) plasma formation followed by shock wave propagation, (2) droplet deformation, (3) sheet breakup through nucleation of holes followed by rapid growth, and (4) complete atomization.

I. INTRODUCTION

Despite the growing focus on renewable energy sources, hydrocarbon fuels maintain their relevance due to their high energy density, well-established infrastructure, versatility, cost competitiveness, energy security, and ongoing technological advancements. Therefore, understanding the atomization of hydrocarbon fuels is relevant for the future development of fuel injection systems. Atomization or the breakup of a liquid stream into droplets is a common occurrence in nature and is extensively utilized in various industrial processes. Apart from internal combustion engines, atomization is employed in activities such as pesticide spraying, spray painting, surface cooling, dispersal of biological agents, and a myriad of other industrial applications.[1–3] The controlled fragmentation of a liquid stream into droplets serves as a versatile and indispensable technique across diverse fields, contributing to the efficiency and effectiveness of numerous industrial processes. Spray formation is also important in medical devices like drug administration,[4,5] inhalers, and nebulizers. Furthermore, manipulation of bubbles is useful in bursting bubbles to break down kidney stones, microsurgery, nanolithography, and many more.[6–9] The properties like surface tension, viscosity, external forces (inertial, acoustic, and electromagnetic force), and non-dimensional groups of those forces are all factors that affect the complex interfacial process of droplet and bubble breakup. Since the droplets are the sub-grid level of a spray, it is crucial to examine the mechanisms of deformation and atomization specific to individual isolated droplets.[10–14]

There are multiple methods to induce the fragmentation of a single droplet. The breakup mechanisms associated with the deformation and fragmentation of the liquid droplet can be achieved by a focused

laser pulse. This approach has been extensively used to study the mechanisms and various breakup patterns. When a high-intensity laser pulse is focused within the droplets and exceeds the specific energy threshold (∼GW/cm^2), it triggers the optical breakdown of the liquid.[15–18] This breakdown manifests as a luminous spark accompanied by intense sound, and it is characterized by the generation of charged particles. A high temperature (∼order of 10^6 K) plasma is formed because of this breakdown, followed by a shock wave propagation.[19–22] Fragmentation of liquid is primarily attributed to the momentum disparity between the liquid and the surrounding gas. This discrepancy in momentum induces a shear instability on the interface between the liquid and gas, giving rise to the formation of wave structures. Subsequently, these liquid waves evolve into thin sheets, which, under the influence of surface tension, develop rims at their free ends.[23] These liquid rims experience transverse instabilities, leading to the formation of fingers that eventually break into ligaments and droplets.[2,24–26] Aerodynamic droplet fragmentation is classified into five distinct breakup modes: multimode breakup,[27,28] vibrational,[29] sheet thinning,[30] catastrophic breakup,[31] and bag breakup.[32,33] Some breakup occurs due to instabilities such as Rayleigh–Taylor (RT) and Rayleigh–Plateau (RP) when the edge of the radially expanded droplets fragments.[2,34–36]

Another significant breakup mechanism involves the formation of holes within waves preceding the development of ligaments. These holes undergo expansion, merging either with each other or with a retracting end rim, ultimately resulting in the rupture of the liquid sheet into droplets.[26,37,38] This additional process underscores the complexity and variety of mechanisms at play in the intricate phenomenon of fluid breakup during atomization. The rupture of the sheet through hole formation is observed in many different investigations.[39–41] Recently Agbaglah[42] revealed the dynamics of the merging of two holes and a single hole with a rim using three-dimensional simulations. Ling *et al.*[43] reported observation of hole formation and subsequent liquid sheet breakup during atomization. A common outcome following hole collision, observed in various configurations, involves the creation of a smooth or rough liquid bridge. This bridge, in turn, detaches into a ligament that either breaks into multiple smaller drops or collapses into a single large drop. The final outcome of the detached ligament depends on its aspect ratio and the associated Ohnesorge number.[44–46] Therefore, investigating the mechanisms leading to ligament formation in the context of hole collisions and understanding the characteristics of the resulting ligaments becomes important for atomization studies.

The primary objective of this study is to investigate the laser-induced optical breakdown inside the hydrocarbon droplets by a focused ultraviolet (UV) laser pulse. Pure component hydrocarbon fuels such as iso-octane and n-hexane are used to understand the secondary atomization and fragmentation of droplets through plasma formation. The rapid phase change properties of hydrocarbon fuels are more prone to form laser-induced plasma within the droplet. To the best of our knowledge, there are no studies conducted on individual hydrocarbon droplets using UV wavelengths. UV light possesses a significantly higher absorption coefficient in hydrocarbon fuels, thus facilitating improved atomization. In this study, we conducted experimental investigations aimed at gaining a thorough understanding of plasma formation, shock wave propagation, droplet deformation, expansion dynamics, and the associated breakup mechanisms. Furthermore, the focus is on understanding single hole formation and its growth, the multiple-hole merging process, and the subsequent rupture of the sheet. Finally, this study elucidates the instabilities (i.e., R–T and R–P) associated with the breakup process.

This paper is structured as follows: After the introduction, Sec. II describes the experimental setup and methodology. In Sec. III, we qualitatively discuss the experimental observations and illustrate various breakup phenomena. Subsection III A focuses on the fragmentation processes of iso-octane droplets, while Subsection III B examines the fragmentation phenomena of n-hexane droplets. Section IV discusses the expansion dynamics, fragment interactions, and instabilities. Finally, Sec. V presents the conclusion.

II. EXPERIMENTAL METHODOLOGY

The schematic of the experimental arrangement to study laser-induced deformation and fragmentation is illustrated in Fig. 1. A Q-switched Nd: YAG laser (Spectra-Physics Quanta Ray) generates a fourth harmonic wavelength of 266 nm with a pulse duration of 5 ns. The pulse repetition rate is 10 Hz, the maximum energy per pulse is 20 mJ, and the laser beam diameter is 10 mm. The laser beam is focused at the center of the droplet using a focusing lens (high power doublet Achromat with a focal length of 150 mm). The droplets are produced using a microliter syringe, needle arrangement at ambient conditions (∼293 K and 30% relative humidity), and levitated in 3D-printed single-axis acoustic levitator. The acoustic levitator consists of an array of transducers at the top and bottom, which operate at a resonance frequency of 40 kHz. The droplets are placed close to the pressure nodes in the acoustic levitator such that the acoustic pressure balances the gravity force to levitate a stable droplet. Once the droplet is stable in the acoustic trap, the laser pulse is aimed to focus in the center of the droplet. The equivalent onset radius of the droplet under levitation is defined as $R_o = (R_a^2 \times R_b)^{1/3}$, where R_a and R_b are the horizontal and vertical radius of the droplet, respectively (see droplet configuration in the inset of Fig. 1).[13,40] Thus, $D_o = 2\,R_o$ represents the onset diameter of the droplet. R(t) is the radius of the expanding drop, which expands over time.

In this study, single droplets of iso-octane and n-hexane are investigated. The properties of the liquids are compared in Table I. The levitated droplet is illuminated with an LED fiber optic lamp (Thorlabs HPlS200). The shadowgraph of the droplet dynamics is captured at 35 and 190 kfps with a resolution of 10 μm/pixel. Droplet dynamics is imaged using a high-speed camera (Phantom, 1 million frames per second as the maximum frame rate) equipped with a microscopic objective lens (Navitor 12X zoom). The high-speed camera and the laser are synchronized using a pulse delay generator. The shadow images of the droplets are post-processed and analyzed using image analysis and Image Pro Plus software. The parameters such as the initial droplet size, secondary drop size (D_s) and its velocity, ligament size, propulsion speed, expansion radius of the sheet/droplet, etc. are measured using Image Pro software and MATLAB. The droplet velocity and propulsion speed are measured by tracking the respective position of droplets/fragments in the successive frames and frame interval. The uncertainty in the measurement of initial droplet diameter (D_0) and laser energy (E_l) reported is not more than 2.5%. The experimental errors (primarily due to pixel identification) together with calibration uncertainties accounted for no more than 2.2% for the ligament and secondary droplet size determination. This experimental setup can be used for newtonion and non-newtonion liquid droplets

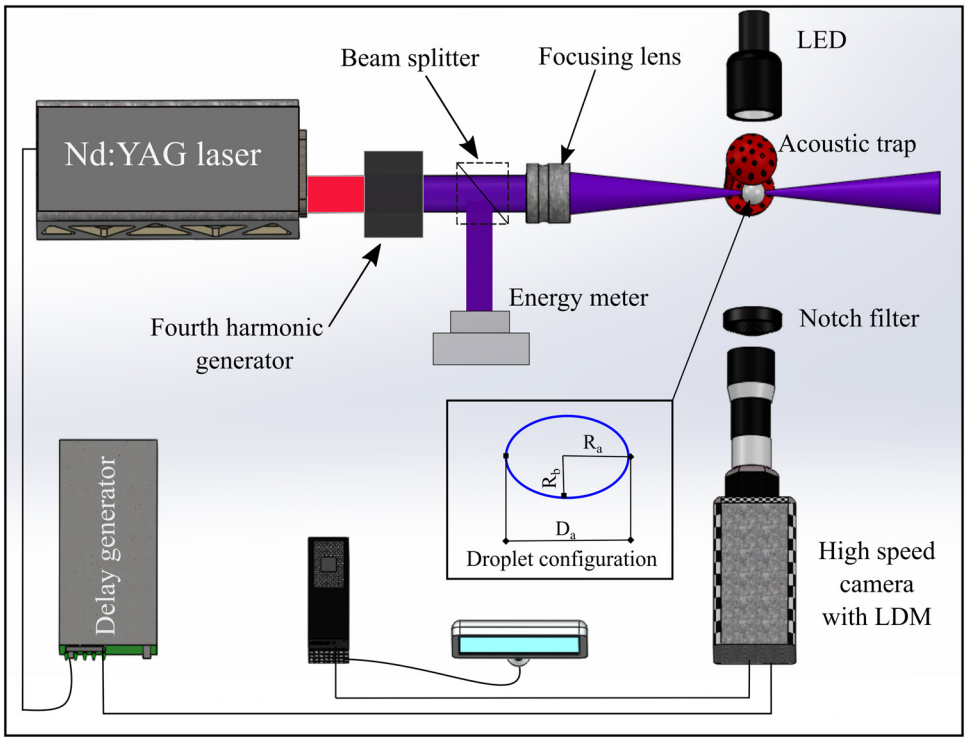

FIG. 1. Schematic top view of the experimental setup for laser-induced fragmentation of levitated droplets.

with viscosities ranged from 0.3 mPa s (Acetone) to 1412 mPa s (Glycerol).

III. RESULTS

The ensuing opto-hydrodynamic behavior during the laser pulse-droplet interaction is contingent on the energy absorption characteristics. The dynamics of the droplet during this interaction is primarily dictated by the energy distribution of the incident laser and the properties of the liquid droplet. Upon focusing the laser within the droplet, a fraction of the energy is absorbed by the droplet, while the remainder is transmitted. The absorbed energy initiates plasma formation, leading to simultaneous expansion and fragmentation of the droplet. The residual energy is carried away by the ensuing shock wave. This study omits consideration of energy losses attributed to radiation, reflection, and scattering, given that their combined contribution has been reported to be less than one percent of the incident energy.[21,49]

TABLE I. Properties of the liquids used in this study.[47,48]

Properties	Units	Iso-octane	n-Hexane
Density (ρ), @ 293 K	kg/m^3	691	660
Surface tension (σ), @ 293 K	N/m	0.0187	0.0179
Viscosity, @ 293 K	mm^2/s	0.72	0.45
Boiling point	K	368	342
Specific heat capacity, C_p	kJ/kg K	2.1	2.26
Latent heat of vaporization, ΔH	kJ/kg	308	335
Molar mass, M	g/mol	114	86
Refractive index	···	1.38	1.37

In our experiment, we exercised control over the location and mode of optical breakdown, influencing the direction of sheet formation or the propulsion of fragments. It became evident that the mode of optical breakdown underwent variations based on the properties of the liquid. Regardless of the specific breakdown mode, our observations indicate that the effective breakup of the target droplet occurs when most of the absorbed energy is dedicated to the process of droplet fragmentation. This typically results in the rapid formation of a thin sheet, which subsequently undergoes a swift collapse. The intricacies of these phenomena underscore the importance of fluid properties in shaping the dynamics of optical breakdown and subsequent droplet breakup. The liquid properties play a vital role in driving the fragmentation mechanisms for the hydrocarbon droplets. The results of fragmentation of iso-octane and n-hexane droplet are discussed below along with their mechanisms.

A. Fragmentation of iso-octane droplet

Figure 2(a) shows the bright spot in the droplet due to plasma formation, and the shock wave in Fig. 2(b) indicated as the dim ring. Propagation of an expanding shock wave and vapor mist behind the drop is observed in [Fig. 2(a)]. The expansion velocity of the shock wave is approximately 760 ± 50 m/s with corrections made for the geometrical distortion arising from the curvature of the drop, as reported by Kobel *et al.*[50] This correction accounts for the specific geometric considerations, ensuring accurate measurements of the shock

wave dynamics. Figure 3 displays the time sequences showing the different dynamics of laser-induced fragmentation of iso-octane and droplets at different laser energies. The complete atomization of the iso-octane droplet is depicted in Fig. 3(a). The droplet is fragmented into a cloud of fine secondary drops. The droplet deformation and ligament-mediated breakup are shown in Fig. 3(b). One thick long ligament is formed, which breaks due to instability. Figures 3(c) and 3(d) present time sequences of the dynamic evolution of the hole expansion and merging processes. This visual representation captures the successive stages in the behavior of the holes, including their expansion, the formation of rims, the merging of holes or interaction with straight rims, the emergence of quasi-symmetric liquid bridges, and the subsequent stretching and detachment into ligaments. Capillary and surface waves with the growth of the single hole on the sheet are observed in Fig. 3(c). The merging of multiple holes and their growth is shown in Fig. 3(d), which subsequently breaks the thin sheet, whereafter several secondary droplets are produced. Liquid accumulation at the edges of the circular sheet makes the rim thicker, causing them to collapse under the influence of surface tension, as observed in Fig. 3(e). The detailed laser-induced dynamics of hydrocarbon droplets is discussed in Subsections III A 1–III A 4.

1. Shock wave dynamics and atomization

This section highlights the comprehensive visual depiction of the dynamic interplay of optical breakdown, shock wave dynamics, and plasma-induced droplet fragmentation in a droplet. This provides valuable insights into the intricate phenomena occurring within the droplet under the influence of focused laser pulses. When a laser pulse is focused inside a droplet, optical breakdown occurs. This laser-induced breakdown initiates the radial outward movement of both plasma and shock waves, with multiple shock waves occurring in the case of multimode breakdown. The plasma and shock wave exhibit simultaneous motion for a duration of a few hundred nanoseconds, depending on the pulse energy. Following this period, the shock wave separates from the plasma, carrying away a significant portion of the absorbed energy.[51,52] Consequently, the remaining energy within the plasma contributes to the breakup of the droplet, leading to the generation of fragments that move radially outward behind the shock wave. The shock wave is [Fig. 2(b)] accompanied by the presence of a vapor plume and a mist cloud of vapor and droplets. This mist cloud is observable as a gray-to-black haze. Fragments are propelled just behind the shock wave for a short period.

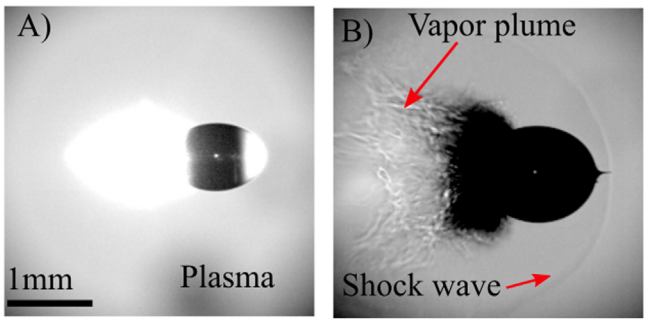

FIG. 2. (a) Plasma formation and (b) shock wave propagation for iso-octane droplets at $t = 5\ \mu s$, $D_0 = 0.49$ mm, and $E_l = 20$ mJ.

The white spot observed at the droplet corresponds to the high-temperature plasma, which is visible in the image. As the shock wave travels into the air, pressure increases behind it. A close examination of the sheet's surface in Fig. 3(a) reveals a structure indicative of a Kelvin–Helmholtz instability. The later dynamics of fragmenting droplets is illustrated in Fig. 3(a). A droplet initially undergoes rapid fragmentation, resulting in the formation of a cloud of fine droplets. The smaller droplets, expelled first, are predominantly situated on the left side of the droplet. The brief duration required for the completion of the fragmentation process distinguishes this regime from the other. The small fragments are ejected at $t = 10\ \mu s$, after the rupture of the droplet wall. These fragments travel initially at a speed of 680 $\pm$ 50 m/s. The speed of the fragments is almost two times faster than the speed of the sound in air at 293 K and 1 atm. We can estimate the maximum size of these fragments by considering the capillary length, λc_f, where the surface tension can counteract the acceleration experienced by the fragments (a_f). It is observed that fragments achieve a velocity of about 380 m/s within 10 μs. Fragments experience an initial acceleration on the order of 10^8 m/s^2. From this, we can estimate the size of the stable fragment d_f as

$$d_f < \lambda c_f = \sqrt{\sigma/\rho\, a_f}, \tag{3.1.1}$$

where $\rho = 691$ kg/m^3 and $\sigma = 0.0187$ N/m are the density and surface tension of the liquid, respectively. Hence, droplets with a diameter exceeding 1 μm are unable to withstand the extreme acceleration, resulting in the blurred appearance of the fragments near the shock front. Due to the limitations of the current experimental setup, these finer details could not be resolved. The overall shape of the fragmenting droplet shown in Fig. 3(a) is discussed in this paragraph. Initially, the right side of the droplet appears smooth, while the left side exhibits a rough surface with a complex pattern. These patterns manifest rapidly as the side expands toward the left. The sheet expands quickly after $t = 5\ \mu s$, becoming apparent again at $t = 10\ \mu s$. This suggests that the sheet undergoes significant shear forces between the relatively still air surrounding the droplet and the outflow from the vaporous explosion. A Kelvin–Helmholtz instability is likely at play in this regime, which is supported by additional experiments. These experiments reveal that, despite being highly corrugated, the sheet remains intact, with the dark structures representing crests of wavy corrugation on the sheet. Fragmentation delay with gradually increasing surface roughness is observed on the right side of the droplet. The wavelength of these structures is significantly smaller than the structures observed in the expanding sheet. The drop continuously deforms and is subsequently fragmented as characterized by a thinner leading edge at $t = 30\ \mu s$. During the stage of deformation of the droplet, the small threads-like structure of the liquid on the drop surface is observed on the right side at $t = 20\ \mu s$. We assume that numerous interactions between multiple waves and the droplet surface take place before the liquid film ruptures. This may be due to cavitation on the droplet surface. Impulsive acceleration of a free surface results in the generation of fast liquid jets from a curved surface.[35,53,54] The fragments are ejected initially at a very high speed and rapidly decelerate to 490 m/s after $t = 15\ \mu s$. A similar study[35,40] has been reported for high velocities of the ejected fragments from the laser-induced cavitation bubbles near a curved free surface.

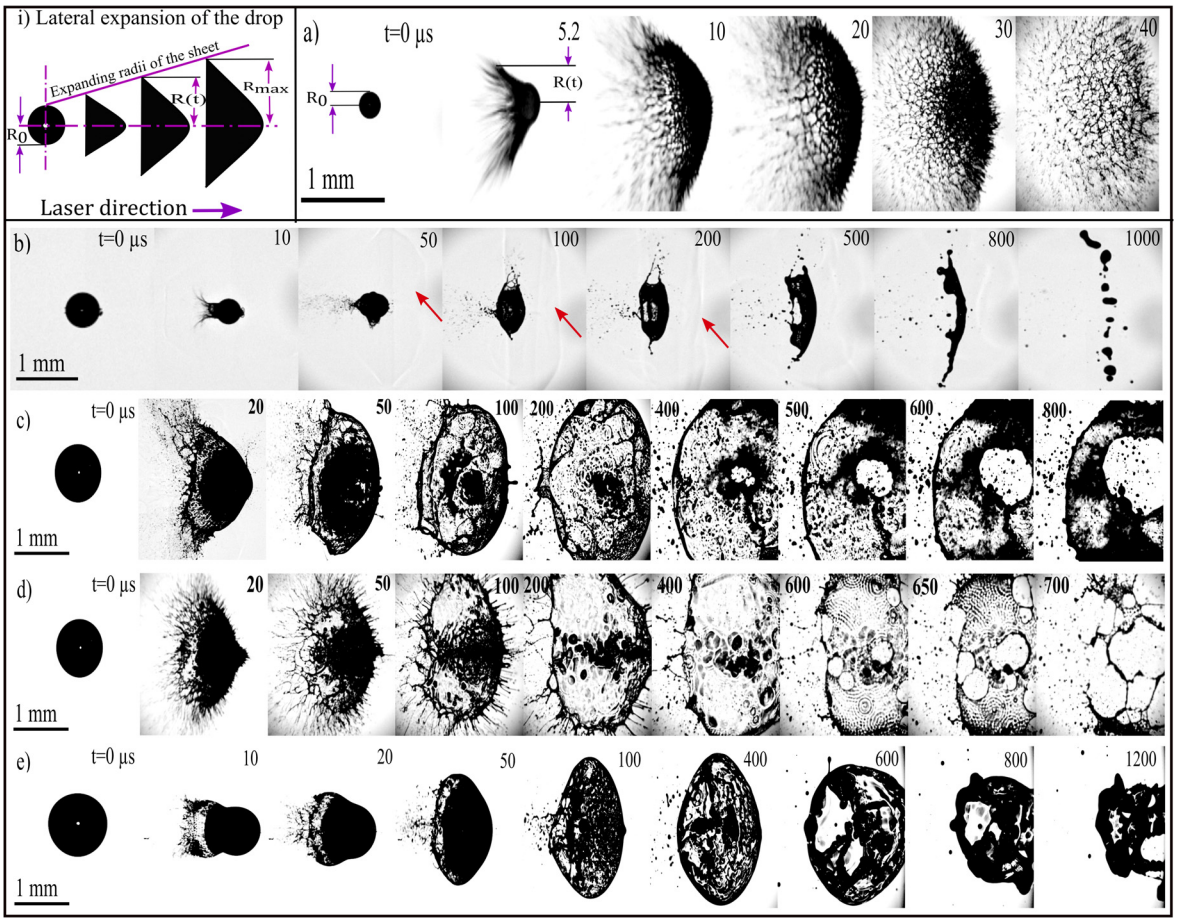

FIG. 3. Overview of laser-induced fragmentation processes of iso-octane droplets; (i) schematic representation of the expanding drop forming a sheet with a lateral expansion radius R(t) from R_0 to R_{max}; (a) complete atomization of the droplet, $D_0 = 0.2$ mm and $E_l = 20$ mJ; (b) ligament-mediated breakup of iso-octane, $D_0 = 0.35$ mm and $E_l = 12$ mJ; (c) sheet breakup through single hole formation within a droplet, $D_0 = 0.55$ mm and $E_l = 17$ mJ; (d) sheet breakup of droplet through multiple holes merging, $D_0 = 0.54$ mm and $E_l = 20$ mJ; (e) stable sheet collapse of a droplet, $D_0 = 0.65$ mm and $E_l = 15$ mJ.

2. Droplet deformation and propulsion

The laser-produced plasma light source used in extreme ultraviolet (EUV) nanolithography extensively uses the laser-induced breakdown (LIB) phenomenon. The droplet deformation and its propulsion were previously reported by Gelderblom *et al.*[37] They observed that the primary driving force behind the observed drop propulsion and deformation is the localized and asymmetric boiling of the liquid, triggered by the absorption of laser energy on the illuminated side of the drop. The absorption of laser energy depends on fluid and laser properties. The resulting vapor recoil pressure is responsible for the deformation and propulsion of the drop [Fig. 3(b)]. The applied laser energy E_l and threshold energy E_{th} required for a liquid layer to achieve the boiling point, so the propulsion velocity V can be obtained as[37]

$$V \sim \frac{E_l - E_{th}}{\rho R^3{}_0 \Delta H} u_T, \tag{3.1.2}$$

where ΔH is the latent heat of vaporization, $u_T = \sqrt{K_B T_b / M}$ is the thermal speed of the expelled vapor, K_B is the Boltzmann constant, T_b is the boiling temperature of the liquid, and M is a molecular mass. From Fig. 3(b), the vapor plume is visible around the droplet and travels in the outward direction represented by the red arrow. This resembles that the evaporation occurs during the energy transfer process. The latent heat of vaporization of iso-octane is very low, which means that early phase change occurs for iso-octane. Along with the vapor plume, a little fine mist is coming out at the proximal side of the droplet. Therefore, the laser energy absorbed by the superficial layer of the iso-octane is sufficient to reach its boiling point. The droplet deforms in the vertical direction, and subsequently, it propels forward. The subsequent vertical stretching of the droplet forms one thick long ligament. The ligament breaks into secondary droplets due to RT instability (at $t = 1000$ μs). The lateral expansion of the drop is correlated with the drop propulsion as[2]

$$\frac{R(t) - R_0}{R_0} \sim We^{1/2} \sim \sqrt{\frac{\rho R_0}{\sigma}} \frac{E_l - E_{th}}{\rho R^3{}_0 \Delta H}, \tag{3.1.3}$$

where the Weber number is written as $We = \rho R_0 V^2/\sigma$, R_{max} is the maximum radius of expanded drop, and R(t) is the radius of the

expanding drop. Therefore, both the propulsion speed and the maximum radius of expansion are directly proportional to the energy of the laser pulse. A comparison of the maximum relative expansion and Weber number is shown in Fig. 4. It shows a best-fit power-law curve based on the average data points for the maximum sheet radii, which compares the square-root exponent of the Weber number (We) as predicted by Eq. (3.1.3). The solid blue line represents the best-fit curve, capturing not only the scaling dependencies [given by Villermaux and Bossa[2] and Gelderblom *et al.*[37]] but also providing a quantitative fit for the average data points. The curve demonstrates a strong correlation with the square-root dependence on the Weber number, particularly at lower and intermediate We values, thus accurately describing the sheet expansion behavior in these regimes. However, at higher "We" values, the radius ratio ($\frac{R_{max}-R_0}{R_0}$) also increases, but at a rate proportional to the square root of We. This scaling is typically in scenarios where inertial forces dominate the surface tension forces, but surface tension still plays a significant role in determining the dynamics of the system. Theoretically, Eq. (3.1.3) shows the dependency of the sheet's expansion radius on the applied and threshold energy. It indicates that when both energies are equal, propulsion is zero. When applied laser energy is greater than threshold energy, we could see some propulsion. Therefore, the specific amount of laser energy is required to get propulsion, here it is called threshold energy. The higher the laser energy, the greater the expansion and propulsion, resulting in a higher Weber number. The inset in Fig. 4 depicts the variation of propulsion speed as a function of the laser energy applied. Here, the propulsion speed is directly measured experimentally from successive frames with respect to the laser energy applied. Hence, it indicates how much the droplet is propelled with different laser energies. As the laser energy increases, the propulsion of the droplet also increases. The formation of the mist along with the vapor plume indicates that the superficial layer of the droplet reaches the boiling point of the liquid. It is an indicative of how much energy is absorbed by the droplet. Figure 2(b) is the condition zero case where we start to observe the mist and vapor plume, which is at 12 mJ laser energy. Below this laser energy, we did not observe mist and vapor cloud, but we observed little propulsion (see insets in Fig. 4). The significant propulsion is observed above 10 mJ and more pronounced at 12 mJ laser energy. Therefore, the threshold energy required for propulsion is approximately 10 mJ, where we see significant propulsion of the droplet. This is also depicted in the inset of Fig. 4, demonstrating good agreement with the experimental observations.

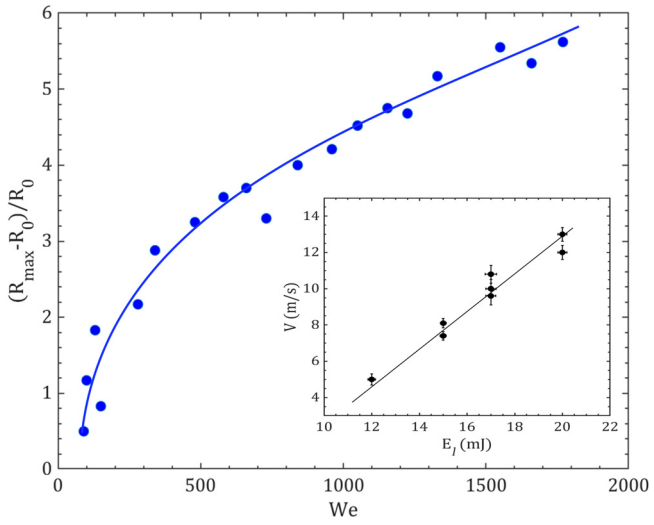

FIG. 4. Maximum expansion of the droplet as a function of the Weber number (We). The solid blue line represents Eq. (3.1.3). The inset represents the variation of the propulsion speed as a function of laser energy. (The solid line is linearly fitted with a pre-factor of 0.6.)

3. Sheet breakup through hole formation

The high-speed shadowgraph images offer valuable insights into the liquid sheet's characteristics and show qualitative features such as radial instability waves, capillary waves, hole formation and its growth, regions of breakup marked by ligaments, and the formation of secondary droplets. Two distinct scenarios are observed: hole–rim merging, corresponding to the interaction involving a single hole in a confined thin liquid sheet [Fig. 3(c)] and hole–hole merging [Fig. 3(d)], representing the dynamics involving two distinct holes in a thin liquid sheet. In both the hole–hole and hole–rim cases, the initial stages involve the expansion of the holes, leading to the formation of rims at their free ends. These rims can either merge with each other or with a sheet's rim, particularly in the case of a bounded liquid sheet. Following this process, a quasi-symmetric liquid bridge emerges, connecting the two holes or the hole and the sheet rim. This characteristic liquid bridge is prominently visible in the seventh image of both Figs. 3(c) and 3(d). As time progresses, the liquid bridge undergoes stretching, concurrently with the continuous growth of the resulting hole after merging. Subsequently, the liquid bridge detaches into a ligament, characterized by blobs formed at its tips. This ligament, depending on its dynamics, has the potential to break into smaller droplets or recoil, ultimately forming a single, larger droplet. The processes highlight the complex and dynamic nature of the liquid sheet evolution after the merging of holes in various configurations. The dimensions of the rim at the onset of the merging process between two holes are identical to the sheet rim. However, in the case of the hole rim, the size of the connecting rim increases.

Notably, during hole–hole merging, the liquid bridge remains straight, while in hole–rim merging, it exhibits an outward curvature. This distinction arises from the differences in shape and size between the toroidal rim and the sheet rim in the hole–rim case. Specifically, the sheet rim possesses only one principal curvature, which is smaller than that of the toroidal rim. Consequently, during merging, the toroidal rim exerts a larger capillary pressure compared to the sheet rim, resulting in the outward curved shape of the liquid bridge. After the collision of the rims bounding two holes or the liquid sheet, the resulting liquid bridge undergoes deformation in the vertical direction (y-axis), leading to the formation of a vertically expanding free liquid sheet. As this occurs, the kinetic energy of the free liquid sheet gradually decreases. Subsequently, under the influence of capillary forces, the upper and lower edges of the vertically expanded liquid bridge recede and eventually merge. Following this, the liquid bridge undergoes deformation in the horizontal direction, forming a horizontally expanding free liquid sheet. This too recedes and merges again. The oscillation of the liquid bridge during these processes has the effect of drawing liquid from the central part of the bridge toward its ends, resulting in the formation of a cone that progressively thickens over time. This observation underscores the influence of geometric factors on the morphological features of the liquid bridge during the merging

of holes in the thin liquid sheet. The expansion of the holes leads to the breakup of the thin sheet. By measuring the expansion velocity (U) of the holes, local planner thickness (h) can be calculated from the Taylor–Culick relation,[55]

$$h = 2\,\sigma/\rho\,U^2. \tag{3.1.4}$$

By considering a surface tension of $\sigma = 0.0187$ N/m and density $\rho = 691$ kg/m^3, the film thickness is calculated as 1.2 μm. By employing mass conservation, it compares to an average film thickness of 4.8 μm, neglecting mass loss on the proximal droplet side. The coalescence of these holes in the sheet gives rise to the creation of liquid ligaments. Subsequently, these ligaments undergo Rayleigh–Plateau instability, resulting in the formation of relatively large droplets compared to the initial ejecta on the left-hand side of the droplet [Figs. 3(c) and 3(d), at t = 20 μs]. The complete rupture of the sheet is observed approximately 700 μs later, in Fig. 3(d), reaching its maximum surface area at t = 600 μs. Figure 5 depicts the sheet breakup through the development of patches (pre-hole and hole) on the sheet. Figure 5(a) shows the single pre-hole and subsequent hole formation on the sheet. Figure 5(b) shows the multiple pre-holes and subsequent holes formed on the sheet. It is observed that the diameter of the patches increases with time. Yet, the growth rate of D_{patch} in the pre-hole regime is notably slow in comparison to the hole regime. To understand the evolution of pre-holes and holes in detail, we monitored the number of pre-holes and holes on the sheet. Figure 6 represents the temporal evolution of the diameter of patches, i.e., $D_{prehole}$ and D_{hole}. The parameters $D_{prehole}$ and D_{hole} exhibit linear variations over time across all the monitored pre-holes and holes on the unstable sheet. The slope of the line representing $D_{prehole}$ is smaller in comparison to that of D_{hole}. This suggests that, even across a wider spectrum of pre-holes and holes, the growth of holes is considerably faster than that of pre-holes. The observed growth rate of holes in the experiment falls within the range of 0.5–2.4 m/s. By assuming the uniform and constant thickness of the sheet, theoretically, the growth rate of the hole can be calculated using Eq. (3.1.4).

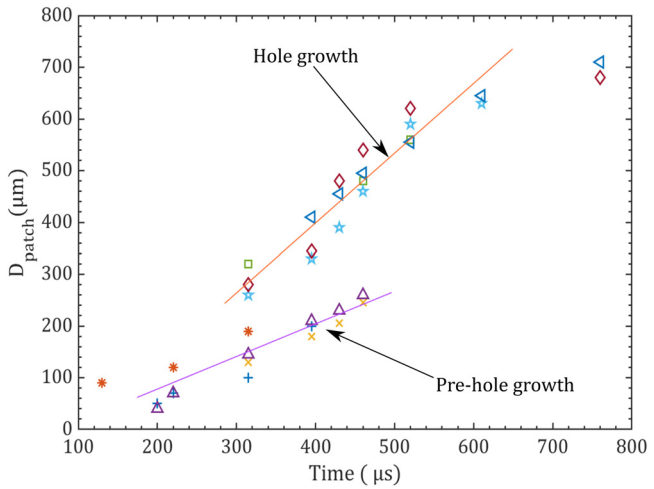

FIG. 6. The variation in diameter of pre-holes and holes over time corresponds to multiple instances of pre-holes and holes. The solid lines are linear fits.

4. Stable sheet collapse

The time sequence of stable circular sheet collapse for the iso-octane droplet is illustrated in Fig. 3(e). In this regime, initial fragments are visible at t = 20 μs due to the initial ejection of the mass at the proximal side of the droplet, typically, its fine mist captured at t = 10 μs. Simultaneously, the droplet stretches vertically and starts to form a circular sheet. The rim becomes notable at an earlier time, t = 50 μs, and becomes more pronounced at t = 100 μs. The sheet experiences substantial and non-uniform radial acceleration as fragments detach from the sheet. By analyzing Fig. 3(e), we can estimate the acceleration of the liquid on the proximal side toward the downstream end of the sheet. The acceleration of the sheet measured is approximately $a_s = 18 \times 10^6$ m/s^2. The sheet achieves the maximum vertical expansion typically at t = 400 μs, and the liquid sheet starts to decelerate. At this point, the liquid starts to accumulate at the edges of the sheet making the rim thicker. The sheet collapses under the influence of the surface tension as can be seen at t = 800 μs. The capillary time $\tau_c = \sqrt{\rho\,R_0{}^3/6\,\sigma}$ is defined by balancing the surface energy with kinetic energy. This timescale represents the duration, during which a hemispherical liquid sheet with a radius R_s collapses to a common center, hence converting surface energy into kinetic energy. For Fig. 3(e),

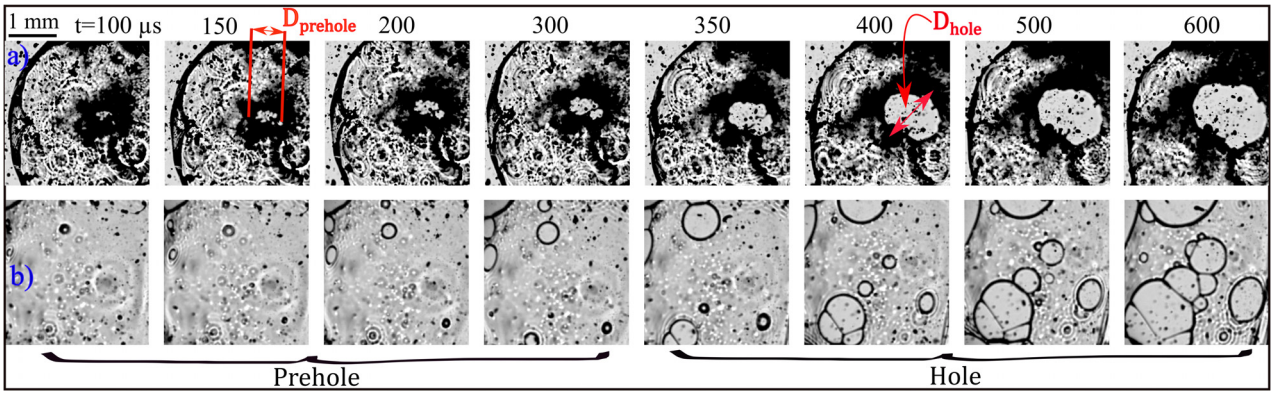

FIG. 5. Sheet breakup through nucleation of the holes in an iso-octane droplet: (a) single hole formation on the liquid sheet, $D_0 = 0.55$ mm and $E_l = 17$ mJ and (b) multiple holes merging on the liquid sheet and its breakup, $D_0 = 0.54$ mm and $E_l = 20$ mJ.

we obtain $\tau_c = 460$ μs, where $R_0 = 0.325$ mm, $\rho = 691$ kg/m^3, and $\sigma = 0.0187$ N/m. It agrees well with the observed sheet lifetime.

B. Fragmentation of n-hexane droplets

Figures 7(a)–7(f) show the initial fragmentation of n-hexane droplets exposed to the laser pulse energy. Similar behaviors are observed compared to iso-octane droplets. The major difference in the results observed for n-hexane droplets is the low angle of opening compared to iso-octane droplets. Fine mist at the distal side and larger fragments at the edges and the rim of the sheet are observed. The fragmentation is influenced by the location of the nucleation. Figure 7(g) represents the graphical view of the laser pulse focus location inside the droplet. Two cases of laser positions are depicted in this figure, where the first case presents the laser position just near the edge of the droplet, and the second case represents the laser position exactly at the center of the droplet. Depending on the position of the laser pulse focus, the angle of fragmentation changes, which subsequently decides its strength. The laser pulse focus position is adjusted by displacing the laser beam focusing lens, which is mounted on a micrometer device to alter the focus position inside the droplet within 50 μm. When the nucleation occurs very near to proximal side surface of the droplet, the smaller opening of the droplet, a relatively low angle of fragmentation is observed [Fig. 7(a)]. As the location of the nucleation moves from proximal to the center of the droplet, the angle of fragmentation increases from narrow to wide [Figs. 7(a)–7(e)].

As the focus location moves toward the center, internal pressure is higher, and the material is ejected at a wider angle. Hence, a wider

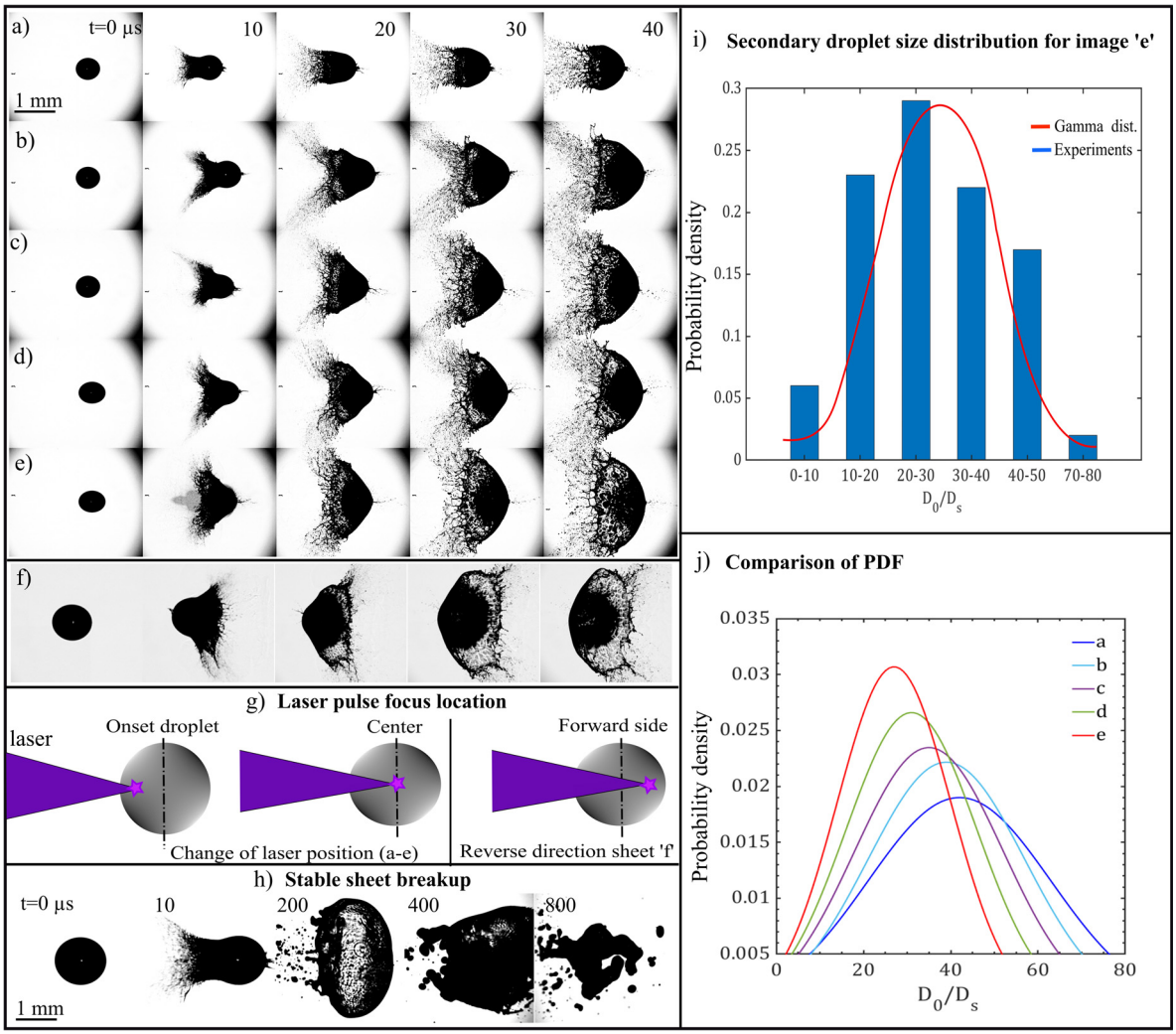

FIG. 7. Initial fragmentation of n-hexane droplet showing a vertical expansion of the droplet concerning laser pulse focus position (a)–(e), $D_0 = 0.53$ mm and $E_l = 17$ mJ. Initial narrow opening for (a) to wide opening for (e) at the proximal side of the droplet, see at $t = 10$ μs. (f) Reverse direction fragmentation of the droplet, $D_0 = 0.60$ mm and $E_l = 17$ mJ. (g) Graphical representation of the laser pulse focus position inside the droplet. (h) Stable sheet breakup of the droplet $D_0 = 0.60$ mm and $E_l = 20$ mJ. (i) Probability density and normalized secondary droplet size distribution of n-hexane droplet depicted in "e." (j) Comparison of probability density function for images (a)–(e).

angle of fragmentation is observed at the center of the droplet [Fig. 7(e)]. When the laser focus is beyond the center point of the droplet, away from the proximal side, the reverse direction of the sheet is observed. Hence, the angle of the fragmentation is opposite to the earlier cases observed [Fig. 7(f)]. After the droplet wall ruptures violent ejection of the vapor mist, fragments is observed. This high-speed ejection is caused by the pressure difference developed between the inside and surrounding of the droplet. A rapid multiphase flow of ejected fragments and vapor mist are observed. This develops an expanding jet flow of gas and fragments. The sheet/main droplet body also gains momentum along with the fast-ejected materials. The center of the mass of the closed system remains stationary. As a combined effect, the main droplet propels forward and expands vertically to form a sheet [Fig. 7(h)]. The sheet is formed after the bulk of the gas comes out of the back side due to a reduction in pressure at the proximal side of the droplet. The secondary droplets produced from fragmented droplets follow a gamma distribution, consistent with the reported literature.[3,56] Villermaux[3] demonstrated that gamma distributions are more effective at fitting drop-size distribution data when compared to distributions such as Poisson or lognormal. Normalized secondary drop size distribution for fragmented droplets for case "e" is shown in Fig. 7(i). Here, D_s is the secondary droplet size generated after the droplet breakup. A similar distribution is observed for all the fragmenting droplets in the present study. The comparison of the probability density function for change in the location of the laser pulse focus is represented in Fig. 7(j). The location of the laser focus with respect to the center of the droplet decides the distribution for the number density and sizes produced fragments. The wider opening of the droplet results in smaller-sized droplets being ejected and more violet fragmentation. In the case of a low angle of opening of the droplet, it produces relatively large secondary-size droplets.

IV. DISCUSSION

This section provides a detailed explanation of the common features and dynamics observed in iso-octane (in Sec. III A) and n-hexane droplets (in Sec. III B). This examines the expansion of the liquid sheet following laser interaction, the formation of shear layers within the flow field, fragment interactions, and the associated instabilities. Understanding these phenomena is crucial for comprehending the behavior of droplets under various conditions and their interactions with external forces, such as laser energy.

A. Expansion dynamics

The stationary spherical droplet of radius R_0 in a quiescent environment, e.g., levitator (considering the minimal effect of radiation force on the droplet, it does not change the acoustic frequency), keeps its original shape. After the laser impact droplet expands and accelerates from R_0 to R_{max} and u_0 to u, respectively, and considering the expanding radius function of $F(u_0, t, \sigma, \ldots.)$, it can be rewritten as[2]

$$R(t) = F(R_0, u_0, t, \sigma, \ldots.). \tag{4.1.1}$$

When the droplet expands, its radius increases and reaches maximum expansion ($R_{max} \gg R_0$). Subsequently, the sheet thickness h decreases, i.e., the aspect ratio h/R_{max} is very small. Thus, the dependent functions for radial velocity and thickness of the expanding drop are $u(R,t)$ and $h(R,t)$, respectively. By considering the slender slope approximation ($|\partial_R h(R,t)| \ll 1$), Euler equation can be written as

$$\rho(\partial_t u + u\partial_R u) = -\partial_R P, \tag{4.1.2}$$

$$R\partial_t h + \partial_R(uhR) = 0, \tag{4.1.3}$$

where $P(R,t)$ is the pressure in the liquid. R = R(t) is the radius of the expanding sheet, which varies with time. There is no interaction with the surrounding gases. The mean radius of the sheet expands until reaching a maximum value, denoted as R_{max}, and depends on u_0, and the corrugation of the sheet rim. These undulations serve as the foundation for radial ligament formation. As the sheet expands, a hole originates on the sheet. This hole extends to the corrugated rim, leading to the breakup of the ligaments and the formation of stable drops.

The entire process, transitioning from the initial drop to stable fragments, completes shortly after the sheet rim begins to recede [i.e., when $\dot{R}(t) < 0$, where $\dot{R} = dR(t)/dt$]. After the impact of the laser, the central liquid is fed to the sheet rim and the collection of radially fragmented particles at the rim by capillary wave action. The mass of liquid is transferred to the rim edge, and concurrently, rim becomes thick (Fig. 8). By considering the initial volume of the drop $\alpha = \pi {D_0}^3/6$, the liquid volume constituting the sheet at time t is represented as[2]

$$\int_{R_0}^{R_{max}} \{2\pi R \times h(R,t)\}\, dR = \alpha - \beta, \tag{4.1.4}$$

where $\beta = \int_0^t [2\pi R(t)\{u(R,t) - \dot{R}\}h(R,t)]dt$ is the net volume accumulated at time t on the rim.When applying momentum conservation at the rim, we consider a system analogous to the propulsion concept given by Tsiolkovsky.[57] It states that the rate of change of the rim inertia is equal to the sum of the momentum it absorbs plus the net force acting on it,[2] expressed as

$$\frac{d}{dt}(mR * \dot{R}) = \varphi u(R,t)R - 2\sigma(R - R_0), \tag{4.1.5}$$

where the φ represents the following terms:

$$\varphi = \rho hR[u(R,t) - \dot{R}], \tag{4.1.6}$$

$$\varphi = \frac{1}{R}\frac{d}{dt}(mR). \tag{4.1.7}$$

The velocity $u(R,t)$ represents the liquid's velocity in the sheet. The force term $2\sigma(R - R_0)$ refers to the initial drop with a radius R_0, which becomes zero when $R = R_0$. Equation (4.1.5) represents the conservation of the mass. The liquid pressure is considered to be the ambient pressure, independent of R. This assumption arises from neglecting interactions with the ambient medium and disregarding viscous stresses. Additionally, there is a correction, accounting for the curvature of the liquid interface as per Laplace's law. While this curvature is weak and diminishes over time for most of the radial curvature, it is more significant at the sheet rim ($R(t) < R_{max}$), where it is approximately of the order $\partial^2 h/\partial^2 R = \alpha/R^4$. The interface dissipates energy, and the internal pressure is not expected to significantly increase compared to its value in the quasi-planar sheet. Thus, the pressure in the liquid remains nearly constant along R(t). By considering the velocity conservation and neglecting pressure gradients, the modified equation for the radius of the expanding sheet is expressed as

$$\ddot{R} + \frac{6}{(\tau_c - t)^2}(R(t) - R_0) + \frac{4}{\tau_c - t}\dot{R} = 0. \tag{4.1.8}$$

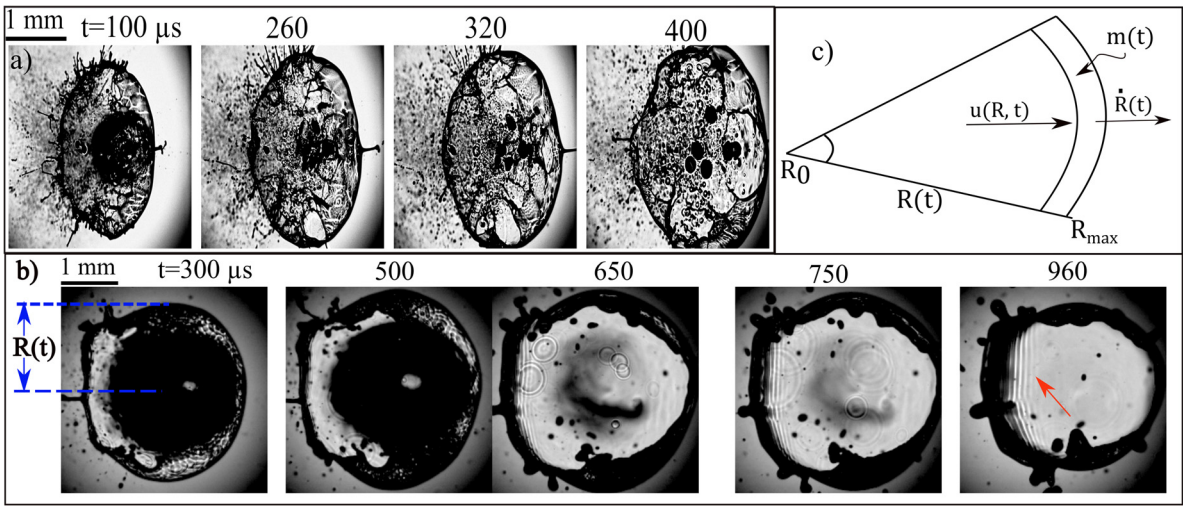

FIG. 8. Expansion dynamics: (a) vertical stretching and radial expulsion from the sheet edge, $D_0 = 0.60$ mm and $E_l = 20$ mJ; (b) expansion of the sheet and gradual accumulation of liquid at the rim, the red arrow indicates the perturbations near the rim edge, $D_0 = 0.65$ mm and $E_l = 17$ mJ; (c) a depiction of the rim with mass per unit arc length, denoted as m(t), attached to the sheet represents the sheet's outer edge with varying distribution of mass along its circumference. The sheet having a mass per unit arc length m (t), velocity u (R, t), and radius R(t) used for mass and momentum balances.[2]

Equation (4.1.8) reveals that the nonlinear dynamics of Eqs. (4.1.2) and (4.1.3) leads to a linearly damped oscillatory motion of the sheet radius. This motion is characterized by a time-dependent frequency and damping factor, representing a balance between the initial drop's inertia and capillary restoring forces as described by Culick's law. The damping term arises from the ongoing transfer of momentum from the sheet to the rim. For the initial case, $R(0) = R_0$ and $\dot{R}(0) = u_0$, the radius of the expanding drop is modified as[2,23,26]

$$\frac{R(t) - R_0}{R_0} = \sqrt{\frac{2\,We_d}{3}}\,\frac{t}{\tau_c}\left(1 - \frac{t}{\tau_c}\right)^2. \tag{4.1.9}$$

This explains an asymmetric on-period oscillatory motion that fits well for various Weber numbers and has a duration of the period $\tau_c = \sqrt{\rho {D_0}^3/6\sigma}$. The capillary time τ_c is defined by balancing the surface energy with kinetic energy. The rescaled Weber number, $We_d = \frac{E_{k,d}}{E_{k,p}}\,We$, depends on the kinetic energy used for deformation, which is expressed as the ratio of deformation to propulsion kinetic energies and corresponding Weber number.[37]

B. Shear layer formation in the fragmenting droplets

The breakup of two similar-sized droplets by a laser pulse with the same laser energy is depicted in Figs. 9(a) and 9(b). It shows the repeatable fluid mechanics, evidenced by the similar sizes of the resulting fragments. This includes the formation of a fine mist on the proximal side and larger fragments originating from the sheet and its edges. Upon closer examination of the images (see Fig. 7), it reveals that the angle at which fragmentation occurs is influenced by the location of the nucleation. In Fig. 9(a), the nucleation is closer to the proximal side. Subsequently, it ruptures through the droplet wall, and mass is ejected at a wider angle as its internal pressure is higher. At this specific condition, we observe two dark stripes on the distal side. These stripes become apparent roughly 20 μs after the laser pulse. After some time, these strips become invisible as they are carried away by turbulent flow. Despite initially resembling two distinct stripes, their actual structure comprises an area with densely packed fine droplet fragments, forming a cone shape. This specific cone shape likely arises from the flow pattern trapping the fragments and increasing their concentration. Such a phenomenon may be attributed to a localized region of reduced gas velocity, such as a shear layer between two dominant flows. The phenomenon of the shear layer formation is well demonstrated in Fig. 9(d).

The fine mist present at the distal side creates a vortex ring formation around the stretched liquid sheet. These vortex rings are observed in Fig. 9(b), approximately 20 μs after the laser pulse, and it is marked by blue arrows. The phenomenon of the vortex ring formation is well depicted in Fig. 9(e). The violent ejection of fragmented drops along with the fine vapor mist is observed as the droplet ruptures by a laser pulse. It creates a fast multiphase flow with higher pressure (P_i) inside the droplet and lower pressure (P_a) in the surroundings, and this phenomenon is demonstrated in Fig. 9(c). This results in the formation of an expanding jet stream comprising both gas and fragmented particles. When regarding the droplet and surrounding air as a closed system, the conservation of momentum dictates that the fast-expelled material imparts momentum to the main droplet/sheet, ensuring that the system's center of mass remains stationary. The sheet is formed as a droplet expands radially outward in the distal direction. This decrease in pressure on the proximal side leads to the suction of gas from the surrounding bulk, contributing to the formation of a sheet at the back. At the rear side of the droplet, the expanding jet and the inflow of gas move in opposite directions, resulting in the formation of a stagnation zone along a stagnation surface where they meet and compete. The dark stripes observed in Fig. 9(a) at time $t = 20$ μs are now understood to correspond to the stagnation surface. At this point, droplets accumulate due to the reduced velocity. Subsequently, as both flows diverge, turbulence is expected to carry these accumulated droplets. This phenomenon is also observed by Avila and Ohl.[40]

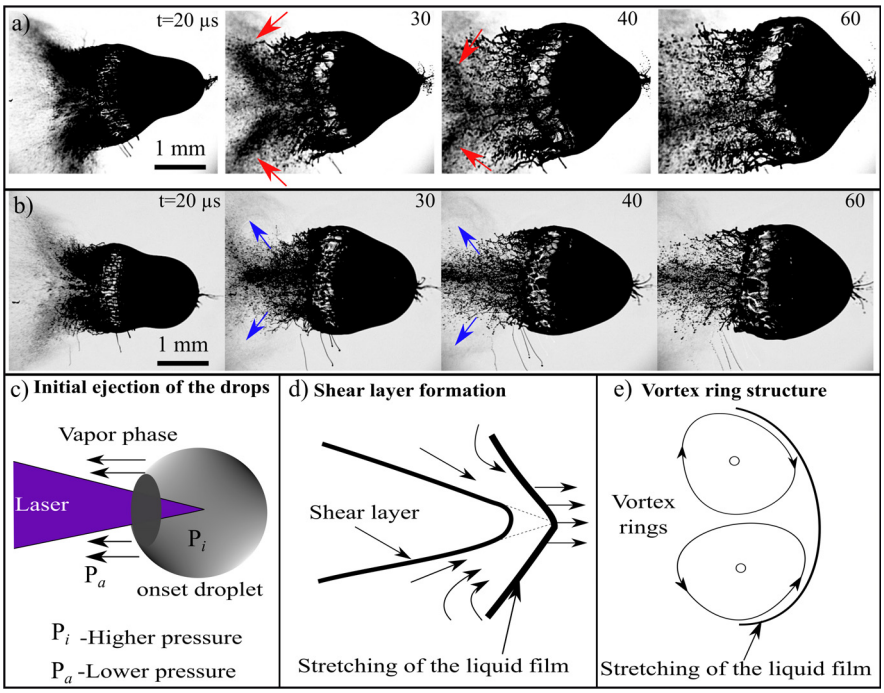

FIG. 9. The initial ejection of the fragments and shear layer formation in the stretching liquid sheet for n-hexane. (a) Shear layer formation, $D_0 = 0.60$ mm and $E_l = 17$ mJ; (b) vortex ring formation around the ejecting drops, $D_0 = 0.60$ mm and $E_l = 17$ mJ; (c) initial ejection of the drops; (d) schematic of shear layer formation; and (e) graphical representation of vortex ring formation around the ejecting drops.

C. Interaction of fragments on the liquid sheet

This section describes the capillary/surface waves' travel due to the fragment's interaction with n-hexane and iso-octane liquid sheet developed. Droplets are captured in a vortical flow at the far end of the sheet. The ejected droplets may be captured in this flow and eventually impact the sheet. It leads to capillary wave generation on the sheet, which subsequently ruptures the sheet. This process deforms the sheet, which eventually leads to fragmentation of the sheet. Figure 10 depicts the successive time frames of the phenomenon of impact of the fragments and eventual capillary/surface wave travel. The droplet sheet is marked with a green arrow to represent different droplets/fragment's impact during successive frames. The impacting droplet has a radius "r" ($r = 2d$), and V_{rel} is the relative velocity between the sheet and impacting droplet. The relative velocity measured is 3.9 m/s, for Fig. 9(a). The Weber number (We) is calculated by comparing the kinetic energy of the droplet and the surface energy of the sheet, $We = \rho r V_{rel}^2/\sigma$. The rupture of the membrane due to fragment impact and surface waves on the surface occurs at We in the range of 4.3–6.8. In most observed cases, we predominantly witness either coalescence or bouncing with $We < 4.3$. There has been no instance of droplet tunneling through the sheet. Figure 10(a) illustrates a scenario where the sheet undergoes deformation but does not rupture, with the impacting droplets tracked by the green-colored arrows. Similarly, Fig. 10(b) depicts the rupture of the membrane by fragment impact.

Ejected secondary droplets/fragments from the liquid sheet impact the same thin sheet. The size of the impacting fragments in these cases ranges from 5 to 10 μm. Fragments/droplets sizes and liquid film thickness are responsible for the breakup of the liquid sheet. The thickness of the thin film is calculated using the Taylor–Culick equation. Liang and Mudawar[61] reported that the thickness of the liquid thin film (h) should be less than 1.5d. For the cases presented in Fig. 9, the thickness lies well within this range. Similar study by Avila and Ohl[40] reported that the film ruptured by a single droplet impact on the same liquid sheet. A detailed study of a droplet's impact on a thin film has been reported by Courbin and Stone.[58] For Weber number $We < 16$, Gilet and Bush[59] observed bouncing and coalescence, a finding that was approximately corroborated by Kim and Wu.[60] A surface tension gradient is observed during the impact of droplets on the sheet of the liquid. Marangoni stresses are observed during the rupture of a thin splash of water because of the impact of ethanol droplets.[35,36] Gilet and Bush[59] used higher surface tension liquid impacting on the soap film, whereas the present study has the same liquid impacts on the thin sheet.

D. Instabilities in the sheet

The liquid ejection through fine jets and surface waviness is observed in earlier cases shown in Figs. 3(c) and 3(d). To get more clarity, the wave generation and jet ejection from the surface are shown in Fig. 11. The smaller mass is displaced from the upper and lower sides of the droplet, which is a potential cause of triggering the R–T instability. The surface undulations are the starting point to the jet formed and fragments ejected from the edges of the sheet. The underlying mechanism for this phenomenon may be similar to jetting resulting from impulse pressure as reported by Antkowiak *et al.*[53] They reported that concentrated flows are directed toward concave regions of the liquid–gas interface, leading to the acceleration of slender jets. When the surface geometry does not align with the impulse pressure distribution, gradients in the liquid are established, leading to the acceleration of the fluid. In our experiments, the fragment's impact and collapse create a rapid inward flow that experiences an abrupt cessation

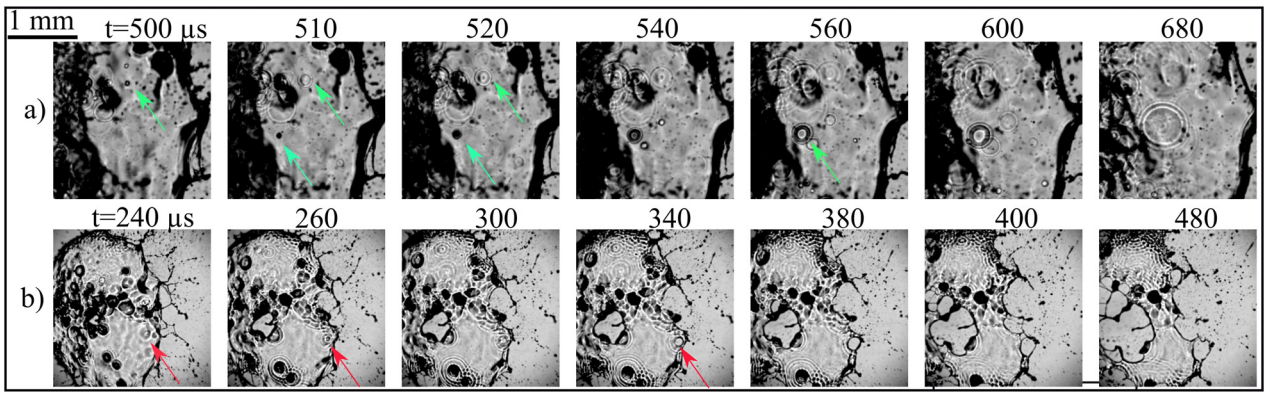

FIG. 10. The fragments impacting the liquid sheet membrane: (a) capillary waves on the surface of n-hexane We = 0.5, D_0 = 0.53 mm, and E_l = 20 mJ and (b) membrane rupture for the iso-octane, We = 4.3, D_0 = 0.53 mm, and E_l = 20 mJ.

and reversal, transforming into an outgoing flow. Neglecting the intricacies of the collapse phase, the final liquid velocity post-collapse can be characterized by the gradient of an impulse pressure. In this case, the surface corrugations deviate from the expected impulse pressure distribution, which usually entails spherical waves originating from the surface of the sheet. The impulse pressure must adhere to the constant pressure boundary condition near the droplet–gas interface for it to serve as a solution to the Laplace equation. Consequently, pressure gradients near the surface are anticipated to meet the boundary condition. Particles near the rim of the sheet belong to a continuously decelerating density interface. Therefore, there is no pressure gradient along the radial direction, hence no net body force.

According to Culick's law, the expansion and recoil dynamics are made under constant pressure, where liquid inertia is balanced by restoring force concentrated at the edge of the rim. Despite the rim of the sheet experiencing deceleration for a significant portion of its development period, the occurrence of a global Rayleigh–Taylor instability in the expanding sheet is improbable. This is because the deceleration primarily affects the fluid particles located in the rim of the sheet, and most of the liquid in the sheet does not undergo this deceleration. As a result, the conditions necessary for a global Rayleigh–Taylor instability, which typically involves a widespread disturbance in the fluid, are not prevalent in the main body of the expanding sheet. Instability is confined to the rim where the deceleration is taking place. The breakup is instigated by individual fragments colliding with the sheet. Notably, the ejected mass resulting from the early jetting phenomenon, as mentioned earlier, serves as the source of these fragments. Importantly, this ejected mass travels at a significantly higher velocity than the expanding sheet, making it improbable for later collisions with the sheet. Bremond and Villermaux[25] have observed the

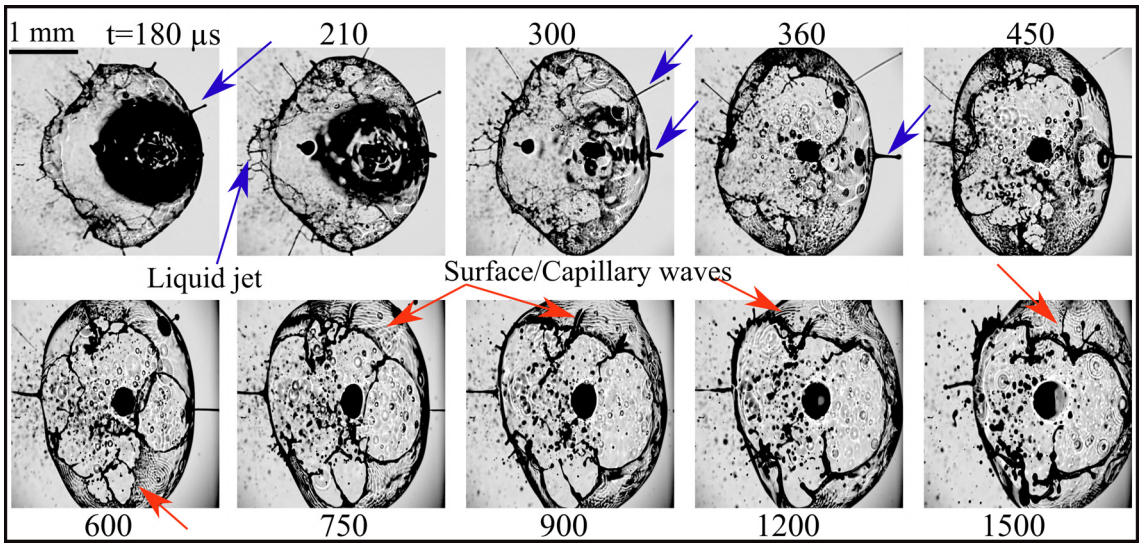

FIG. 11. Liquid jet ejection and surface/capillary wave propagation from the liquid sheet surface of iso-octane. The blue arrow shows the liquid jet ejected from the sheet, and the red arrow shows the surface/capillary waves travel on the sheet surface. D_0 = 0.55 mm and E_l = 20 mJ.

nucleation of holes in micrometer-thick, freely suspended liquid sheets. In their study, an impulsive acceleration of the sheet initiated a Rayleigh–Taylor instability, leading to the development of growing corrugations that ultimately pierced the sheet. The observed number of holes is determined to rise proportionally with the Weber number calculated based on the forward velocity (and consequently the acceleration) of the sheet. Simultaneously, the characteristic rupture time exhibited a decrease with the Weber number.[25]

In our experiments, immediately after the laser impact, the spherical drop experiences an acceleration, denoted as $a \sim V/\tau_e = R_0/\tau_c\tau_e\, We^{1/2}$ on the timescale of matter ejection τ_e. During this initial phase ($t \leq \tau_e$), a potential Rayleigh–Taylor instability may be triggered on the drop and then evolve concurrently with the developing sheet on the inertial timescale ($\tau_e \sim R_0/V$) until the sheet eventually breaks on a timescale (τ_c). The Weber number is a direct scale for impulsive acceleration if the given R_0, τ_c, and τ_e remain constant in each system. From the experiments, it is observed that the number of holes increases, and breakup time decreases with an increase in Weber number. This is aligned with the R–T sheet breakup, which is described by Bremond and Villermaux.[25] The gradual accumulation of the liquid takes place at the rim edge. Hence, the rim rapidly becomes thick compared with the sheet. The total volume accumulated at the rim is expressed as

$$\frac{\pi^2 b^2}{2} R_{\max} = \alpha - \int_{R_0}^{R} 2\pi R \times h(R,t)\, dR, \tag{4.2.1}$$

where b is the rim diameter and $R \sim \sqrt{W_e}\,\frac{t}{\tau_c}\left(1-\frac{t}{\tau_c}\right)^2 \approx \sqrt{W_e}\,\frac{t}{\tau_c}$. The rim is unstable due to capillary action at the rim similar to the Rayleigh–Plateau mechanism.[25] The destabilization timescale gives the timescale for Rayleigh–Taylor instability, which is represented by the capillary timescale, $\tau_{RT} \sim \sqrt{\frac{\rho b^3}{\sigma}} \sim \tau_c\, We^{-3/8} \ll \tau_c$. This timescale is much smaller than the overall sheet-drop transition period τ and smaller than the typical time t as $R/\dot{R} \sim t$. Hence, it does not affect its development time $t/\tau_c > We^{-3/8}$. Shortly thereafter, the rim undergoes rapid destabilization due to corrugations along the sheet edges. The sheet loses stability, leading to its breakage, and ligaments emerge from the sheet edges. Despite $\ddot{R} \neq 0$, the pressure along the sheet remains constant up to $R = R_{\max}$. However, the rim experiences deceleration, accompanied by a corresponding body force pushing fluid particles radially outward. This force induces the R–T mechanism locally at the rim. During the deceleration phase of the rim, perturbations are created with wavenumber k.[25] The perturbations are carried by fluid particles that experience geometric separation as the sheet expands.[2,35,38] The characteristic wave number k_r makes ω^2 extremum, and then this R-T instability mode growing fast on the rim is expressed by Klein *et al.*[26] as $k_r \sim (a\,\rho/\sigma)^{1/2}$.

E. Overview of the present study

The study on the fragmentation of pure component droplets, specifically iso-octane and n-hexane, demonstrates distinct breakup behaviors between the two types of fuel. Both fuels exhibit a vapor mist along with a vapor plume at the proximal side of the droplet, which indicates a rapid phase change occurring in these fuel droplets. However, there are slight differences in the breakup dynamics of the two fuels. For n-hexane droplets, the vapor mist generally appears as a gray haze. This suggests a more controlled and less violent breakup process. In contrast, iso-octane droplets undergo complete atomization, indicating a much more aggressive and thorough fragmentation. When comparing the physical properties of the two hydrocarbons (refer to Table I), it is evident that iso-octane has higher values in terms of viscosity, density, and boiling point compared to n-hexane. These properties contribute to the differing breakup mechanisms observed in the study. Upon closer inspection, it is evident that while both fuels exhibit similar features in terms of deformation, instabilities, and fragment interaction, the primary difference lies in their expansion dynamics. Iso-octane, with its higher viscosity, tends to have a relatively wider expansion during the breakup process compared to n-hexane droplets. This is visually represented in Fig. 7. Consequently, the effective angle of fragmentation for n-hexane droplets is observed to be less than that for iso-octane droplets. The breakup behavior of iso-octane is characterized by an unstable sheet breakup leading to complete atomization, demonstrating a more violent fragmentation process. On the other hand, n-hexane predominantly exhibits a stable sheet breakup in most cases, indicating a less aggressive and more controlled disintegration of the droplet. This contrast in breakup behaviors is directly linked to the inherent physical properties of the two fuels, influencing their respective fragmentation mechanisms during the rapid phase change process.

V. CONCLUSIONS

This study reveals the distinct characteristics of laser-induced plasma, shock wave dynamics, and the accompanying breakdown of iso-octane and n-hexane droplets. The hydrodynamic response of the droplet to the laser impact, encompassing propulsion, deformation, expansion, and fragmentation, is comprehensively elucidated.

1. Droplet transformation due to energy transfer: initially, plasma is formed, a shock wave evolved out, and simultaneously, a drop propels forward due to high laser pulse impact. The droplet undergoes radial expansion, transforming into a thin sheet.
2. Fragmentation mechanisms: the interaction between the laser and the droplet results in fragmentation through several mechanisms. Initially, the droplet transforms into a sheet. Subsequently, the breakup of the rim is influenced by two laser-controlled parameters: the Weber number (propulsion due to laser-induced recoil pressure, which depends on laser energy) and the distribution of kinetic energy between expansion and propulsion. Furthermore, the interaction between the fragments and the sheet induces small disturbances on the sheet surface, which gradually grow over time, leading to the breakup of the sheet. Finally, the laser-droplet interaction also governs overall thickness variations in the expanding sheet, which can arise from irregularities in the laser beam profile or laser-induced non-uniformities in sheet kinematics, such as liquid jetting from the center.
3. Dynamics of hole evolution and its merging: additionally, forward acceleration of the sheet leads to its destabilization through the nucleation of holes, ultimately resulting in sheet breakup. Hole merging in thin liquid sheets exhibits complex dynamics. Two scenarios are observed: hole–rim merging involving a single hole in a confined thin liquid sheet, and hole–hole merging with two distinct holes. These processes involve initial stages of hole expansion and rim formation, leading to subsequent merging or

interaction with a sheet rim in the case of a bounded liquid sheet. The curvature of the liquid bridge differs between hole–hole and hole–rim merging due to variations in toroidal and sheet rim characteristics, influencing capillary pressure and bridge shape.
4. Instabilities: fragmentation in both systems arises from two Rayleigh–Taylor instabilities caused by the acceleration of the drop in two orthogonal planes and at different time scales. The drop expands radially into a thin sheet with a decelerating rim, and the unstable sheet expels ligaments and eventually breaks under Rayleigh–Plateau instability.
5. Properties: both fuels show rapid phase changes, with n-hexane forming a gray haze and iso-octane undergoing complete atomization. Higher viscosity of iso-octane leads to wider expansion and relatively higher opening angle compared to n-hexane. More violent breakup of iso-octane is observed compared to n-hexane, which generally exhibits stable sheet breakup.

ACKNOWLEDGMENTS

Y. N. Mishra gratefully acknowledges the Swedish Research Council for the financial support of Grant No. IPD2018-06783 and the funding from the Adlerbertska Research Foundation. V. S. Jagadale gratefully acknowledges support from the Erasmus+ International Credit Mobility Program. Financial support was obtained from Carl Tryggers Foundation (CTS 19:132).

AUTHOR DECLARATIONS

Conflict of Interest

The authors have no conflicts to disclose.

Author Contributions

Vishal S. Jagadale: Conceptualization (equal); Data curation (equal); Formal analysis (equal); Investigation (equal); Methodology (equal); Software (equal); Validation (equal); Writing – original draft (equal); Writing – review & editing (equal). **Devashish Chorey:** Data curation (equal); Investigation (equal); Writing – review & editing (equal). **Mats Andersson:** Supervision (supporting); Writing – review & editing (equal). **Devendra Deshmukh:** Conceptualization (equal); Methodology (equal); Project administration (equal); Supervision (equal); Validation (equal); Writing – review & editing (equal). **Dag Hanstorp:** Funding acquisition (equal); Project administration (equal); Supervision (equal); Validation (equal); Writing – review & editing (equal). **Yogeshwar Nath Mishra:** Conceptualization (equal); Funding acquisition (equal); Project administration (equal); Supervision (equal); Writing – review & editing (equal).

DATA AVAILABILITY

The data that support the findings of this study are available from the corresponding authors upon reasonable request.

REFERENCES

[1]A. H. Lefebvre and V. G. McDonell, *Atomization and Sprays*, 2nd ed. (Taylor & Francis, 2017).
[2]E. Villermaux and B. Bossa, "Drop fragmentation on impact," J. Fluid Mech. **668**, 412–435 (2011).
[3]E. Villermaux, "Fragmentation," Annu. Rev. Fluid Mech. **39**, 419–446 (2007).
[4]J. Di, J. Kim, Q. Hu, X. Jiang, and Z. Gu, "Spatiotemporal drug delivery using laser-generated-focused ultrasound system," J. Controlled Release **220**, 592–599 (2015).
[5]N. Saklayen, M. Huber, M. Madrid, V. Nuzzo, D. I. Vulis, W. Shen, J. Nelson, A. A. McClelland, A. Heisterkamp, and E. Mazur, "Intracellular delivery using nanosecond-laser excitation of large-area plasmonic substrates," ACS Nano **11**(4), 3671–3680 (2017).
[6]V. Venugopalan, A. Guerra, K. Nahen, and A. Vogel, "Role of laser-induced plasma formation in pulsed cellular microsurgery and micromanipulation," Phys. Rev. Lett. **88**(7), 078103 (2002).
[7]M. S. Hutson and X. Ma, "Plasma and cavitation dynamics during pulsed laser microsurgery in vivo," Phys. Rev. Lett. **99**(15), 158104 (2007).
[8]F. Torretti, J. Sheil, R. Schupp, R. Hoekstra, O. O. Versolato, A. J. Neukirch, and J. Colgan, "Prominent radiative contributions from multiply-excited states in laser-produced tin plasma for nanolithography," Nat. Commun. **11**, 2334 (2020).
[9]C. Yao, R. Rahmanzadeh, E. Endl, Z. Zhang, J. Gerdes, and G. Hüttmann, "Elevation of plasma membrane permeability by laser irradiation of selectively bound nanoparticles," J. Biomed. Opt. **10**(6), 064012 (2005).
[10]A. H. Lefebvre and D. R. Ballal, *Gas Turbine Combustion*, 3rd ed. (Taylor and Fransis group, 2010).
[11]E. Villermaux and B. Bossa, "Single-drop fragmentation determines size distribution of raindrops," Nat. Phys. **5**(9), 697–702 (2009).
[12]S. Lyu, V. Mathai, Y. Wang, B. Sobac, P. Colinet, D. Lohse, and C. Sun, "Final fate of a Leidenfrost droplet: Explosion or takeoff," Sci. Adv. **5**(5), eaav8081 (2019).
[13]D. C. K. Rao and S. Basu, "Atomization modes for levitating emulsified droplets undergoing phase change," Exp. Fluids **61**(2), 41 (2020).
[14]V. S. Jagadale, D. C. K. Rao, D. Deshmukh, D. Hanstorp, and Y. N. Mishra, "Modes of atomization in biofuel droplets induced by a focused laser pulse," Fuel **315**, 123190 (2022).
[15]R. G. Meyerand and A. F. Haught, "Gas breakdown at optical frequencies," Phys. Rev. Lett. **11**(9), 401–403 (1963).
[16]S. A. Ramsden and P. Savic, "A radiative detonation model for the development of a laser-induced spark in air," Nature **203**(4951), 1217–1219 (1964).
[17]C. G. Morgan, "Laser-induced breakdown of gases," Rep. Prog. Phys. **38**, 621–665 (1975).
[18]A. L. Klein, W. Bouwhuis, C. W. Visser, H. Lhuissier, C. Sun, J. H. Snoeijer, E. Villermaux, D. Lohse, and H. Gelderblom, "Drop shaping by laser-pulse impact," Phys. Rev. Appl. **3**(4), 044018 (2015).
[19]P. K. Kennedy, D. X. Hammer, and B. A. Rockwell, "Laser-induced breakdown in aqueous media," Prog. Quantum Electron. **21**(3), 155–248 (1997).
[20]G. Sinibaldi, A. Occhicone, F. Alves Pereira, D. Caprini, L. Marino, F. Michelotti, and C. M. Casciola, "Laser induced cavitation: Plasma generation and breakdown shockwave," Phys. Fluids **31**(10), 103302 (2019).
[21]J. Noack and A. Vogel, "Laser-induced plasma formation in water at nanosecond to femtosecond time scales: Calculation of thresholds, absorption coefficients, and energy density," IEEE J. Quantum Electron. **35**(8), 1156–1167 (1999).
[22]D. C. K. Rao, A. P. Singh, and S. Basu, "Laser-induced deformation and fragmentation of droplets in an array," Int. J. Multiphase Flow **148**, 103925 (2022).
[23]E. Villermaux and C. Clanet, "Life of a flapping liquid sheet," J. Fluid Mech. **462**, 341–363 (2002).
[24]J. C. Lasheras and E. J. Hopfinger, "Liquid jet instability and atomization in a coaxial gas stream," Annu. Rev. Fluid Mech. **32**, 275–308 (2000).
[25]N. Bremond and E. Villermaux, "Bursting thin liquid films," J. Fluid Mech. **524**, 121–130 (2005).
[26]A. L. Klein, D. Kurilovich, H. Lhuissier, O. O. Versolato, D. Lohse, E. Villermaux, and H. Gelderblom, "Drop fragmentation by laser-pulse impact," J. Fluid Mech. **893**, A7 (2020).
[27]H. Hirahara and M. Kawahashi, "Experimental investigation of viscous effects upon a breakup of droplets in high-speed air flow," Exp. Fluids **13**(6), 423–428 (1992).
[28]L. P. Hsiang and G. M. Faeth, "Drop deformation and breakup due to shock wave and steady disturbances," Int. J. Multiphase Flow **21**(4), 545–560 (1995).
[29]A. Shraiber, A. M. Podvysotsky, and V. V. Dubrovsky, "Deformation and breakup of drops by aerodynamic forces," Atomization Sprays **6**, 667–692 (1996).

[30]Z. Liu and R. D. Reitz, "An analysis of the distortion and breakup mechanisms of high speed liquid drops," Int. J. Multiphase Flow **23**(4), 631–650 (1997).
[31]D. D. Joseph, J. Belanger, and G. S. Beavers, "Breakup of a liquid drop suddenly exposed to a high-speed airstream," Int. J. Multiphase Flow **25**(2), 1263–1303 (1999).
[32]M. Jalaal and K. Mehravaran, "Fragmentation of falling liquid droplets in bag breakup mode," Int. J. Multiphase Flow **47**, 115–132 (2012).
[33]G. T. Theofanous and J. G. Li, "On the physics of aerobreakup," Phys. Fluids **20**(5), 052103 (2008).
[34]A. L. Yarin, "Drop impact dynamics: Splashing, spreading, receding, bouncing," Annu. Rev. Fluid Mech. **38**, 159–192 (2006).
[35]S. T. Thoroddsen, T. G. Etoh, and K. Takehara, "Crown breakup by Marangoni instability," J. Fluid Mech. **557**, 63–72 (2006).
[36]S. T. Thoroddsen, K. Takehara, T. G. Etoh, and C. D. Ohl, "Spray and microjets produced by focusing a laser pulse into a hemispherical drop," Phys. Fluids **21**(11), 112101 (2009).
[37]H. Gelderblom, H. Lhuissier, A. L. Klein, W. Bouwhuis, D. Lohse, E. Villermaux, and J. H. Snoeijer, "Drop deformation by laser-pulse impact," J. Fluid Mech. **794**, 676–699 (2016).
[38]P. Marmottant and E. Villermaux, "Fragmentation of stretched liquid ligaments," Phys. Fluids **16**(8), 2732–2741 (2004).
[39]N. Dombrowski and R. P. Fraser, "A photographic investigation into the disintegration of liquid sheets," Math. Phys. Sci **247**(924), 101–130 (1954).
[40]S. R. G. Avila and C. D. Ohl, "Fragmentation of acoustically levitating droplets by laser-induced cavitation bubbles," J. Fluid Mech. **805**, 551–576 (2016).
[41]D. Chaitanya Kumar Rao and S. Basu, "Phenomenology of disruptive breakup mechanism of a levitated evaporating emulsion droplet," Exp. Therm. Fluid Sci. **115**, 110086 (2020).
[42]G. G. Agbaglah, "Breakup of thin liquid sheets through hole-hole and hole-rim merging," J. Fluid Mech. **911**, A23 (2021).
[43]Y. Ling, D. Fuster, S. Zaleski, and G. Tryggvason, "Spray formation in a quasi-planar gas-liquid mixing layer at moderate density ratios: A numerical closeup," Phys. Rev. Fluids **2**(1), 014005 (2017).
[44]R. M. S. M. Schulkes, "The contraction of liquid filaments," J. Fluid Mech. **309**, 277–300 (1996).
[45]A. A. Castrejón-Pita, J. R. Castrejón-Pita, and I. M. Hutchings, "Breakup of liquid filaments," Phys. Rev. Lett. **108**(7), 074506 (2012).
[46]J. Hoepffner and G. Paré, "Recoil of a liquid filament: Escape from pinch-off through creation of a vortex ring," J. Fluid Mech. **734**, 183–197 (2013).
[47]L. Zigan, I. Schmitz, A. Flügel, M. Wensing, and A. Leipertz, "Structure of evaporating single- and multicomponent fuel sprays for 2nd generation gasoline direct injection," Fuel **90**(1), 348–363 (2011).
[48]S. Werner and W. Meier, "Measurement of evaporation of hydrocarbon droplets by laser absorption spectroscopy," Appl. Phys. B **126**(1), 13 (2020).
[49]R. Joarder, G. C. Gebel, and T. Mosbach, "Two-dimensional numerical simulation of a decaying laser spark in air with radiation loss," Int. J. Heat Mass Transfer **63**, 284–300 (2013).
[50]P. Kobel, D. Obreschkow, A. De Bosset, N. Dorsaz, and M. Farhat, "Techniques for generating centimetric drops in microgravity and application to cavitation studies," Exp. Fluids **47**(1), 39–48 (2009).
[51]A. P. Singh, U. P. Padhi, R. Joarder, and A. Roy, "Spatio-temporal effect of the breakdown zone in the laser-initiated ignition of atomized ethyl alcohol-air mixture," Appl. Energy **247**, 140–154 (2019).
[52]T. X. Phuoc, "Laser-induced spark ignition fundamental and applications," Opt. Lasers Eng. **44**(5), 351–397 (2006).
[53]A. Antkowiak, N. Bremond, S. Le Dizès, and E. Villermaux, "Short-term dynamics of a density interface following an impact," J. Fluid Mech. **577**, 241–250 (2007).
[54]I. R. Peters, Y. Tagawa, N. Oudalov, C. Sun, A. Prosperetti, D. Lohse, and D. Van Der Meer, "Highly focused supersonic microjets: Numerical simulations," J. Fluid Mech. **719**, 587–605 (2013).
[55]F. E. C. Culick, "Comments on a ruptured soap film," J. Appl. Phys. **31**(6), 1128–1129 (1960).
[56]S. Kooij, R. Sijs, M. M. Denn, E. Villermaux, and D. Bonn, "What determines the drop size in sprays?," Phys. Rev. X **8**, 031019 (2018).
[57]K. E. Tsiolkovsky, "The exploration of cosmic space by means of reaction devices," *Reviewer In Philippine Literature* (Scientific Review, 1903), Vol. 5, pp. 1–23.
[58]L. Courbin and H. A. Stone, "Impact, puncturing, and the self-healing," Phys. Fluids **18**(9), 91105 (2006).
[59]T. Gilet and J. W. M. Bush, "The fluid trampoline: Droplets bouncing on a soap film," J. Fluid Mech. **625**, 167–203 (2009).
[60]I. Kim and X. L. Wu, "Tunneling of micron-sized droplets through soap films," Phys. Rev. E **82**(2), 026313(2010).
[61]G. Liang and I. Mudawar, "Review of mass and momentum interactions during drop impact on a liquid film," Int. J. Heat Mass Transfer **101**, 577–599 (2016).